Image-based finite element modeling of air flow and thermal transport in Al-fiber-sintered porous materials

S. Kawai[a, *] and I. Watanabe[b]

[a] *Innovation Center, Mitsubishi Materials Corporation, 1002-14 Mukohyama, Naka, Ibaraki 311-0102, Japan*

[b] *Materials Modeling Group, Data-driven Materials Research Field, Center for Basic Research on Materials, National Institute for Materials Science, 1-2-1 Sengen, Tsukuba, Ibaraki 305-0047, Japan*

[*]Corresponding Author: Tel: 81(0)-29-295-5705, Fax: 81(0)-29-295-5740

E-mail: skawai@mmc.co.jp

Abstract

In this study, the pressure drop and heat transfer in a heat-transfer tube filled with a sintered porous medium comprising Al fibers were investigated using computational fluid dynamics (CFD) simulations. We reconstructed the sintered fibrous porous structure and generated a computational mesh using X-ray computed tomography, and the simulated pressure drop and heat transfer agreed well with the results reported by Enoki et al. The differences in both the form coefficient and the permeability between two different samples can be reasonably explained by the differences in both the specific solid surface area and the porosity. Further, the CFD simulations indicated that thermal conduction of the Al solid phase enhanced the heat exchange between the air and Al fibers. To examine the effect of solid-phase thermal conduction, we generated a model of a heat-transfer tube having an ideal wire mesh structure, in which we introduced the interfacial thermal conductivity between Al fibers and the inner tube wall as additional factors. We also performed CFD simulations with four different shell-

region thicknesses and found that even a very narrow gap of 5 to 10 μm heavily impacted the heat-exchange performance because of the low thermal conductivity of the shell region.

Keywords: Heat transfer; Pressure drop; Computational fluid dynamics; X-ray computed tomography; Image-based finite element modeling.

1. Introduction

Efficient heat transfer and thermal recovery are required to ensure both the reliability and stability of devices such as heat exchangers and heat sinks for the cooling of integrated circuit chips and power electronics, as well as to improve their energy efficiencies. To enhance the heat-transfer characteristics of such devices, porous media can be added, and this approach has drawn significant attention. Crucially, porous materials exhibit favorable thermal and hydrodynamic performance for use in industry, for example, as heat exchangers, heat sinks, and thermal energy storage units. Generally, porous materials have large heat-transfer areas per unit volume, and maximizing this parameter is key to enhancing the heat-transfer rate. However, large heat-transfer areas often cause large pressure drops owing to frictional losses of the flowing fluid. Therefore, a precise understanding of the pressure drop and amount of heat transferred within devices, such as heat-transfer tubes, containing porous materials is crucial for achieving optimal and efficient device function.

To date, different forms of porous materials, including metal foams, fibers, and particle beds, have been used to enhance the heat-transfer performance. Of these, metal foams have a disordered and interconnected network structure with a tortuous flow path. Kim et al. [1] experimentally examined the effect of Al foam on the flow and convective heat transfer in an asymmetrically heated channel. In addition, Noh et al. [2] experimentally investigated both the fluid flow and heat transfer in an annulus containing high-porosity Al foam. Further, Adabi et al. [3] experimentally measured the heat transfer and pressure drop in a small Cu tube filled with Cu foam.

Woven wire gauzes have also been used in heat-transfer equipment and processes. For example, Tian et al. [4] experimentally examined the effect of the orientation of the air flow on the overall pressure drop and heat-transfer performance of brazed Cu textile meshes with periodic cellular topologies; Wu et al. [5] experimentally measured the pressure drop through woven metal screens and formulated an empirical equation to describe their friction characteristics; and Kolodziej et al. [6] experimentally investigated the fluid flow and heat transfer in a tubular apparatus composed of stacked wire gauzes. In addition, Iwaniszyn et al. [7] performed computational fluid dynamics (CFD) simulations of the fluid flow and heat transfer of a single wire gauze using the representative volume element (RVE) model.

Heat-transfer tubes filled with solid particles have also been frequently employed because they can be manufactured relatively easily by filling a channel or tube with particles and powder. Jiang et al. [8] experimentally investigated the fluid flow and forced convective heat transfer in a plate channel filled with glass or metallic spherical particles. In a different study, they also performed similar experimental investigations on microchannel heat exchangers and microporous heat exchangers [9]. Later, Jeng et al. [10] experimentally investigated heat transfer in an asymmetrically heated rectangular channel filled with brass beads, and Zhang et al. [11] analyzed the heat transfer associated with forced convection in a heat-transfer tube filled with granular porous media.

Fibrous porous materials have also been studied where the porous media are composed of fibers or fiber-like particles. For example, Tadrist et al. [12] reported the thermal and hydrodynamic performance of two kinds of fibrous materials: randomly stacked fibers and commercial Al foam, whereas Enoki et al. [13,14] conducted experiments on the heat transfer and pressure drop in the Al heat-transfer tube filled with sintered Al fibrous high-porosity media. Panerai et al. [15] experimentally measured the pressure gradient across a sample composed of a commercial fibrous carbon media to obtain a benchmark dataset of the permeability properties. Raudenský et al. [16] reported a new type of heat exchanger,

chaotised flexible polymeric fiber heat exchangers (CFPFHEs), where the flexible polymeric hollow fibers were used as heat transfer elements.

In the studies mentioned above, correlations between the friction factor or heat-transfer coefficient and the fluid velocity (or the Reynolds number) were proposed to understand the heat-transfer performance associated with forced convection [1–3,5–10,13,14]. However, the proposed correlation formulas were somewhat different for several coefficient values for each kind of porous media, and the reasons underlying this difference have been discussed considering porosity, specific surface area, equivalent pore diameter, strut diameter, and tortuosity differences. Particularly, the equivalent pore diameter is a crucial parameter used to estimate the characteristic length scale for the interstitial fluid flow. Dietrich et al. [17] proposed an estimation procedure for the equivalent pore diameter using the specific surface area via magnetic resonance imaging for ceramic open-cell foams, and they also proposed correlations between the equivalent pore diameter and the nominal pore per inch number provided by the foam manufacturer.

Compared to woven wire gauze and open-cell foams, in the case of fibrous porous structure, insufficient information concerning the correlation between the equivalent pore diameter and geometrical parameters such as the fiber diameter, fiber length, porosity, and specific surface area has been elucidated. The equivalent pore diameter is closely related to the tangle level of large number fibers, which depends on the processing conditions such as fiber filling and sintering. For these reasons, several earlier studies employed the square root of the permeability as the characteristic length scale instead of the equivalent pore diameter [2,13,14]. However, tedious and time-consuming experimental measurements are required to estimate the permeability. CFD simulations may therefore be used as alternative methods for experimentally estimating the permeability within fibrous porous materials.

Recently, computational power has increased significantly, and various numerical studies of fluid flow through idealized porous structures have been conducted. For example,

Boomsma et al. [18] performed CFD simulations of the fluid flow through an idealized open-cell metal foam (OCMF) using the RVE model. Kopanidis et al. [19] performed a CFD simulation for the heat transfer associated with fluid flow through an idealized high-porosity OCMF, in which eight cells composed of six tetrakaidekahedra and two dodecahedra were used as the representative open-cell volume. Bai et al. [20] performed a CFD simulation of fluid flow through a simplified OCMF comprising a one-sphere-centered tetrakaidecahedron structure. Tang et al. [21] also performed a pore-scale CFD simulation of the heat transfer and fluid flow characteristics in tetrakaidekahedron OCMF. Nie et al. [22] numerically investigated the pressure drop and heat transfer through an OCMF having a three-dimensional (3D) structure created by Laguerre–Voronoi tessellation. Yang et al. [23] performed a pore-scale CFD simulation of the fluid flow and heat transfer through a high-porosity OCMF under rotating conditions; specifically, a radially rotating channel filled with a Weaire–Phelan foam cell was numerically modeled. Konduru et al. [24] also presented an experimental and numerical studies on porous heat exchangers composed of Kelvin-cell-based metal foam (KMF) at high temperature by considering the interplay among conduction, convection, and radiation. Recently, triply periodic minimal surface (TPMS) structure has drawn significant attention toward the novel convective heat-transfer enhancement [25-29], in which both the method to precisely control TPMS lattice structure and the effects of TPMS lattice parameters on the thermo-hydraulic performance were reported.

Furthermore, recent numerical studies have focused on the effects of the metal foam strut shape on convective heat transfer and pressure drop performance. For example, Moon et al. [30] performed CFD simulations of the fluid flow and heat transfer through a modified KMF with circular or elliptical struts. In addition, Calati et al. [31] further examined the fluid flow and heat transfer through a KMF with elliptical struts and discussed the effect of the strut orientation with respect to the main fluid-flow direction on the pressure drop and heat transfer coefficient. Finally, Ambrosio et al. [32] numerically examined the effects of strut

130 shape on the convective heat transfer and pressure drop in ideal and real foams using the
131 RVE model.
132 Recently, the fluid-flow and heat-transfer rates in foams having realistic pore
133 structures have been numerically calculated using CFD combined with X-ray computed
134 tomography (CT) measurements. For example, Torre et al. [33] performed laminar CFD
135 simulations of the fluid flow through an Al foam. Using the Darcy–Forchheimer law [34,35]
136 and micro-CT image-based CFD simulations, they estimated both the permeability and form
137 coefficient. Ranut et al. [36] numerically investigated the fluid flow and heat transfer in an Al
138 metal foam using CFD simulations combined with the X-ray CT technique. In their study, a
139 small representative cubic volume was extracted as the RVE model. Meinicke et al. [37]
140 performed CFD simulations of the fluid flow inside a porous SiO_2 glass sponge and also
141 carried out experimental measurements of the fluid velocity using the particle image
142 velocimetry technique. In their CFD simulations, the RVE of the sponge structure was
143 numerically modeled using high-resolution X-ray CT, and the calculated velocity fields were
144 compared with their own experimental measurements. Dixit et al. [38] performed CFD
145 simulations of the fluid flow and heat transfer through an open-cell Al foam and reported
146 small deviations between the experimental and calculated results that arose from the small
147 computational elemental size extracted from the original foam sample. Wang et al. [39]
148 investigated the fluid flow and heat transfer inside reticulated porous ceramics numerically
149 using unsteady-state CFD simulations combined with X-ray CT data, and they discussed the
150 local thermal equilibrium during the transient conjugate heat-transfer process. Liu et al. [40]
151 numerically investigated a pore-scale convective heat transfer characteristics in a Bentheimer
152 sandstone core sample, where the numerical model was reconstructed with micro-CT image
153 data. Recently, Zhang et al. [41] performed a pore-scale simulation of forced convection heat
154 transfer in metal foams with uniform and gradient porosities, where CFD models were
155 reconstructed with an X-ray CT scan of copper foam samples and the CFD model with

gradient porosity was constructed merging two separate models with different porosities numerically. They examined the effect of the gradient orientation on the heat transfer performance. Kuhlmann et al. [42] developed an open-source based workflow for converting CT data to volume meshes appliable for finite volume method based CFD simulation. In recent numerical studies [43−45], the Lattice Boltzmann Method (LBM) was used to calculated fluid flow through metal foams reconstructed with micro-CT data, since the LBM is a quasi-molecular method and considered as powerful tool for microscopic or mesoscopic fluid flow phenomena.

Most studies mentioned above used a RVE model with symmetrical or periodic boundary conditions. Few studies have investigated the fluid flow associated with heat transfer over the entire structure of a realistic porous structure. However, Sadeghi et al. performed a full-field CFD simulation of the gas flow over the entire structure of open-cell foams [46] and regular catalytic monolithic structures [47]. In their studies, the open-cell foam and ceramic honeycomb structures were numerically generated based on X-ray CT data. They also performed experimental measurements of the fluid-flow pattern using magnetic resonance velocimetry. The calculated spatially resolved flow patterns corresponded well with their experimental measurements. Although the RVE model can reduce computational time, it does not consider the effects of a heterogeneous pore distribution within the porous medium on both the pressure drop and heat-transfer characteristics. In particular, when a porous medium is manufactured by filling a container with fibers or particles, they are confined by the container inner wall, which affects the porosity distribution within the medium; this is the so-called wall-confinement effect [48,49]. A full-field CFD simulation is needed to examine the wall-confinement effect on the fluid flow associated with heat transfer.

Furthermore, in real heat-transfer tubes containing fibrous porous media, the tube walls often serve as a heat sink or heat source, and the interface between the inner tube wall

182 and the fibers is closely associated with the solid-phase thermal conduction path between the
183 porous structure and the heat sink or source region. Few studies have thus far investigated the
184 heat-transfer performance within the porous media associated with the solid-phase thermal
185 conduction path from the heat sink or source region. However, Zavattoni et al. [50] recently
186 numerically examined the effect of "contact or non-contact" between the porous structure and
187 parting plate, which serves as the heat sink or source region. In their CFD model, a relatively
188 wide gap of 0.25 mm was employed due to the difficulty of welding two different ceramic
189 materials. Their study focused on the heat-transfer tube in relatively high-temperature
190 environment (600 to 1000 K) where the porous ceramic structures and parting plate or tube
191 were manufactured separately. Relatively wide clearance inevitably was observed when the
192 porous structures and parting plate or tube were coupled together in the final device form.
193 Conversely, metal materials such as Cu and Al have been often employed as heat-transfer
194 tubes in a relatively low-temperature environment (around 300 to 500 K). These metal heat-
195 transfer tubes can be manufactured in a combined state using a sintering process, where a
196 very narrow gap region (10^{-5} to 10^{-6} m) between the porous structure and tube inner wall is
197 expected to be present. To date, no studies have focused on the effects of such a narrow gap
198 region between the porous structure and the heat sink or source region on the heat-transfer
199 performance of such systems.
200 In this study, we applied an X-ray CT-based CFD model to heat transfer associated
201 with fluid flow through the entire structure of a heat-transfer tube filled with a sintered
202 fibrous high-porosity medium for the quantitative estimation of both the permeability and
203 form coefficient. The entire structure of the actual heat-transfer tube filled with sintered
204 fibrous high-porosity medium was reconstructed and modeled using the X-ray CT technique.
205 The calculated pressure drop and amount of heat transferred were compared with the results
206 of previous measurements by Enoki et al [13,14]. In their study, the heat-transfer tube was
207 manufactured by the same process as that in the present study. Following the precedent set by

208 earlier experimental studies, the outer wall of the heat-transfer tube in the present CFD model
209 used was defined as the heat sink.
210 Furthermore, the Al heat-transfer tube filled with sintered fibrous high-porosity
211 media has very large specific fluid surface area $S_{v,\,fluid}$ of 2000 to 3000 m^{-1}, which is
212 approximately two-times larger than those reported in earlier CFD simulations using the X-
213 ray CT technique ($S_{v,\,fluid}$ of 300 to 1500 m^{-1} [31,32,36,39]). This is the first study to apply a
214 CFD model with X-ray CT to an entire Al heat-transfer tube filled with high-porosity media
215 whose $S_{v,\,fluid}$ value is over 2000 m^{-1}, which is the first novelty of the present study. Higher $S_{v,}$
216 $_{fluid}$ values inevitably produce very narrow pores and highly irregular surface shapes for the
217 porous structure composed of sintered fibers. In the present study, the finite element method
218 was selected for analysis because of its high suitability for the 3D modelling of the irregular
219 shapes of sintered fibrous high-porosity structures. Both the permeability and form
220 coefficient were estimated using the calculated results and the Darcy–Forchheimer law. The
221 effects of the differences in the porosity and the specific solid surface area between the
222 different Al heat-transfer tube samples on both the permeability and form coefficient were
223 discussed according to the Ergun equation. The second novelty of the present research is to
224 numerically examine and discuss relationship between the Ergun parameters and X-ray CT
225 based porous structure.
226 Further, to discuss the heat-transfer performance of the heat-transfer tube containing
227 a fibrous high-porosity medium, a heat-transfer tube having an idealized wire mesh structure
228 was generated, which has a $S_{v,\,fluid}$ value of 3500 m^{-1}. The effect of a very narrow gap region
229 on the order of 10^{-5} to 10^{-6} m between the fibers and the tube inner wall on the heat-transfer
230 performance was numerically examined, and the shell conduction model was employed to
231 achieve simulations with limited computational costs. The third novelty of this study is to
232 numerically examine such narrow gap effects on the heat transfer performance.
233

2. CFD model

In the present study, a YXLON Cheetah μHD multifocus X-ray CT instrument was used to scan the sample. Two Al heat-transfer tubes having sizes of ∅18 × 25 mm and ∅18 × 50 mm filled with a sintered fibrous high-porosity medium having a porosity of approximately 80 % were manufactured at Mitsubishi Materials Corporation (MMC Innovation Center, SAITAMA-SHI, Japan). Aluminum fiber having a diameter of approximately 300 μm was used as the fibrous material. The inner and outer diameters of the heat-transfer tube were approximately 18 and 20 mm, respectively. The process used for the manufacture of the filled Al heat-transfer tube was the same as that used in previous experimental studies [13,14]. To reconstruct 3D images and generate a computational mesh from cross-sectional image data, the Amira–Avizo program [51] was employed.

Figure 1 shows a cross-sectional image of the Al heat-transfer tube filled with sintered fibrous high-porosity medium obtained using X-ray CT. In this figure, the white and black colors correspond to the solid Al and fluid air phases, respectively. The 3D image of the Al heat-transfer tube filled with sintered fibrous high-porosity media was then reconstructed from the stack of cross-sectional two-dimensional images containing voxels having sides measuring 55.4 μm. A total of 400 cross-sectional images were used to generate the CFD model of the tube having a size of ∅18 × 25 mm, whereas 900 cross-sectional images were employed for the sample having a size of ∅18 × 50 mm. The specific fluid surface area $S_{v,\,fluid}$, specific solid surface area $S_{v,\,solid}$, and porosity ε are listed in Table 1, which were estimated using the CFD model.

Figure 2 shows the generated CFD model setup and boundary conditions for the Al heat-transfer tube filled with sintered fibrous high-porosity media. This model setup was determined based on the previous experimental studies by Enoki et al. [13,14]. Figure 2 also shows the cross-sectional plane used to visualize the temperature and fluid-flow velocity contours. The CFD model was set up within the ANSYS FLUENT framework. In this study,

Eqs. (1), (2), (3) and (4) are the continuity, momentum, and energy equations and were solved numerically using the single-phase steady-state laminar model [19,30].

Continuity equation:

$$\nabla \cdot (\rho \mathbf{u}) = 0. \quad (1)$$

Momentum equation:

$$\nabla \cdot (\rho \mathbf{u}\mathbf{u}) = -\nabla p + \eta \nabla^2 \mathbf{u}. \quad (2)$$

Energy transport equation in the fluid region:

$$\nabla \cdot \left(\rho c_p \mathbf{u} T\right) = \nabla (k \nabla T). \quad (3)$$

Energy transport equation in the solid region:

$$\nabla (k \nabla T) = 0. \quad (4)$$

Here, ρ expresses the fluid density, $\mathbf{u}$ = (u,v,w) is the fluid velocity vector, p is the pressure, η is the viscosity, c_p is the specific heat capacity, T is the temperature, and k is thermal conductivity. Unlike in earlier numerical studies [7,22-24,31-33,36,37,39,46,47], the dependencies of the density, viscosity, specific heat capacity, and thermal conductivity of the fluid on temperature were determined using Eqs. (5)–(8), respectively [52].

$$\rho = -2.331 \times 10^{-8} \times T^3 + 3.409 \times 10^{-5} \times T^2 - 1.819 \times 10^{-2} \times T + 4.196 \quad (5)$$

$$\eta = 4.317 \times 10^{-8} \times T + 5.529 \times 10^{-6} \quad (6)$$

$$c_p = -2.112 \times 10^{-8} \times T^4 + 3.353 \times 10^{-5} \times T^3 - 1.909 \times 10^{-2} \times T^2 + 4.692 \times T + 582.9 \quad (7)$$

$$k = 7.128 \times 10^{-5} \times T + 4.196 \times 10^{-3} \quad (8)$$

The material properties of the solid Al phase are listed in Table 2 and were assumed to be constant [31].

A fixed temperature of 273.15 K was applied to the outer tube wall surface as a boundary condition. On the thick inlet and outlet side walls of the heat-transfer tube, the heat flux was assumed to be zero, and a no-slip boundary condition was applied to the wall surfaces. The mass-flow inlet boundary condition was adopted at the inlet interface, and a

286 constant mass-flow rate of 0.125–1.5 g/s was set. A fixed air temperature of 473.15 K was
287 applied to the inlet surface. A mass-flow outlet boundary condition with a specified mass-
288 flow rate was applied at the outlet interface.
289 Preliminarily, the grid independence was tested for the same geometrical model with
290 different computational grid sizes. Figure 3 compared the pressure drop along the heat-
291 transfer tube length *L* and the averaged outlet air temperature among three CFD models with
292 different computational grid sizes for the same heat-transfer tube having size of ∅18 × 25
293 mm. In these calculations, the air mass-flow rate was varied between 0.25 and 1.5 g/s. We
294 examined three different computational meshes composed of 10 million, 25 million, and 40
295 million computational cells. As seen in Figure 3(a), the calculated pressure drops in 10
296 million cells were lower than those obtained in both 25 million and 40 million ones in each
297 air flow velocity. Similarly, the calculated averaged outlet air temperatures in 10 million cells
298 were lower than those obtained in both 25 million and 40 million ones in each air flow
299 velocity. Using the calculated results in 40 million cells as a benchmark, the relative error
300 increased with the air flow velocity, which became up to 9 % for pressure drop and over 1 %
301 for outlet air temperature. Contrarily, both the pressure drops and outlet air temperatures
302 obtained in 25 million cells, corresponded well with those obtained in 40 million cells: the
303 averaged relative error was estimated to be within 2.5% for pressure drop and 0.5 % for outlet
304 air temperature. Thus, we considered that approximately 25 million and 50 million
305 computational cells were appropriate for the present CFD simulations for the heat-transfer
306 tubes having sizes of ∅18 × 25 mm and ∅18 × 50 mm, respectively. Figure 4 shows the
307 generated surface mesh for the heat-transfer tubes having sizes of ∅18 × 25 mm, and the
308 typical visualizations of cross-sectional computational mesh in XY, XZ, and XZ mid-planes.
309 In Figures 4(b)-(d), the red and blue colors correspond to the solid Al and fluid air phases,
310 respectively.
311

3. RESULTS

3.1 Numerical evaluation of the Al heat-transfer tube filled with a sintered fibrous high-porosity medium

Figure 5 shows the computed air-flow patterns and temperature contours in the Al heat-transfer tube having a size of ∅18 × 25 mm. For these calculations, the air mass-flow rates were 0.5 and 1.0 g/s respectively. Figure 5(a) shows the streamlines of the air flow through the heat-transfer tube, and the air temperature is shown as colored contours. The complicated path line indicated the intricate porous structure of the sintered Al fibers, which remain unchanged with change in the air mass-flow rate. The average air temperature on the outlet surface was estimated to be 280 K at a flow rate of 0.5 g/s, whereas it was estimated to be 295 K at a flow rate of 1.0 g/s, suggesting that the temperature of the downstream air increased with the increase in the air mass-flow rate because of the limited heat exchange. Figures 5(b) and 5(c) show the contours of the Al fiber and air temperatures, respectively. Notably, as the air-flow rate increased, the temperature of the Al fibers increased, particularly in the upstream region. This indicates that the Al fibers receive a significant amount of heat, and, thus, the solid-phase thermal conduction cannot cool the fibers sufficiently.

Figure 6 shows typical examples of the calculated cross-sectional contours for the Al heat-transfer tube having a size of ∅18 × 25 mm for air mass-flow rates of 0.5 and 1.0 g/s respectively. Figure 6(a) shows the cross-sectional temperature contours, where the temperatures of the air and solid Al phases are shown. Figure 6(b) shows the cross-sectional contours of the fluid velocity. The fluid velocity vector is shown as a black arrow, and the solid Al phase is shown in white. Figure 6(a) shows the Al fiber portion as a relatively lower-temperature contour owing to the solid-phase thermal conduction toward the outer wall of the heat-transfer tube, indicating that solid-phase thermal conduction is a key factor in achieving a high degree of heat exchange. Figure 6(b) shows the intricate air-flow stream, as indicated by the black arrow. As shown, the air passes through the narrow gap between the Al fibers

with a relatively higher velocity and then bifurcates after collision with the downstream Al fiber. Therefore, the Al fiber should receive a large amount of heat via heat exchange during collisions with the air molecules.

At higher air flow rates, both the air and Al fibers had higher temperatures within the heat-transfer tube owing to the limited heat exchange. Figure 6(b) shows that both local high- and low-velocity regions are scattered within the heat-transfer tube as a result of the heterogeneous distribution of the gap regions. Air having a local low-velocity in the wide gaps is expected to flow through the medium without sufficient heat exchange, whereas air with a local high-velocity in the narrow gaps is expected to flow through with a high degree of heat exchange. In addition, the local high-velocity air flow inside the narrow gaps contributes to a larger pressure drop owing to frictional losses. Thus, fabricating a heat-transfer tube without extremely narrow or wide gaps is desirable for enhancing heat exchange with lower pressure drop. However, in the manufacturing process used in this study, the gap distribution in the heat-transfer tube cannot be controlled. Therefore, the reproducibility of both the pressure drop and heat-transfer performance is reduced, and this is a key disadvantage of the sintered fibrous high-porosity medium used in this study.

3.2 Comparison of CFD simulation and literature results

Figure 7 shows a comparison of the calculated pressure drops with those reported in Ref. [13]. In these calculations, the air mass-flow rate was varied between 0.125 and 1.5 g/s for heat-transfer tubes having sizes of ∅18 × 25 and ∅18 × 50 mm. The vertical axis indicates the pressure drop from the inlet to the outlet divided by L. The black circles and black squares indicate the experimental results reported in Ref. [13]. As shown in Figure 7, both the measured and calculated pressure drops can be expressed by the following Forchheimer-extended Darcy equation [34,35].

$$\frac{\Delta P}{L} = \frac{\eta}{K}u + C\rho u^2 \quad (9)$$

Here, u expresses the air-flow velocity, C is the form coefficient, and K is the permeability. The first term is the pressure drop arising from viscous effects, whereas the second term is the pressure drop arising from inertial effects. The red and blue dotted lines are the approximations to experimental results obtained using Eq. (9) for heat-transfer tubes having sizes of ∅18×25 and ∅18×50 mm, respectively. For the heat-transfer tube having a size of ∅18×50 mm, our calculated results (blue line with square symbols) corresponded well with the experimental results (black squares with blue dotted line). However, a slight deviation between the calculated and measured values was observed for the tube having a size of ∅18×25 mm. We speculate that the reason for this discrepancy is that the heat-transfer tube samples used in this study were not the same as those used in Ref. [13]. According to Eq. (9), both C and K were estimated from the CFD simulations. The estimated values are listed in Table 3, where experimental measurement data obtained by Enoki et al. [13] are also included. The C values estimated by the present CFD simulation corresponded well with the measured values, whereas the estimated K values via the present CFD simulation were slightly larger than the measured values. The deviation of the pressure drop between the calculated and measured values was therefore ascribed to this difference in permeability as a higher permeability in the CFD simulation corresponds to a decrease in the pressure drop, as seen in Eq. (9). Next, we examined the effects of the differences in the geometrical parameters of the porous structure on the differences in both C and K estimated using the calculated results for two different heat-transfer tube samples of ∅18×25 and ∅18×50 mm. It is well-known that Eq. (9) can be rewritten as the following Ergun equation [53-55].

$$\frac{\Delta P}{L} = \alpha \frac{{S_{v,solid}}^2(1-\varepsilon)^2}{\varepsilon^3}\eta u + \beta \frac{S_{v,solid}(1-\varepsilon)}{\varepsilon^3}\rho u^2 \quad (10)$$

Here, α and β express the Ergun parameters for viscous and inertial terms, respectively. According to Tables 1 and 3, (α, β) can be estimated as (2.86, 0.35) for ∅18 × 25 mm and

388 (3.43, 0.33) for ∅18 × 50 mm. Similar values of β were obtained between ∅18 × 25 mm and
389 ∅18 × 50 mm, whereas the values of α differed from one another. This result indicates that
390 the way the air flows through the Al heat-transfer tube of ∅18 × 25 mm is quite similar to
391 that in the ∅18 × 50 mm tube, and α is more sensitive to slight differences in $S_{v,\,solid}$ and ε
392 than β. Furthermore, the values of (α, β) estimated by the present CFD simulations differ
393 from the empirical values of (4.17, 0.292) estimated by Ergun [55], whereas they agree well
394 with the results of an earlier study by Inayat et al. [53], who estimated (α, β) as (3.65, 0.31)
395 around a porosity of 0.84 in the case of cylindrical struts. In a different study, Inayat et al.
396 also proposed the semi-empirical correlation for reticulated ceramics foams [56] which
397 estimated (α, β) as (2.60, 0.30) around a porosity of 0.84. These comparisons suggests that
398 the tortuous flow trajectories associated with the sintered fibrous high-porosity media are
399 clearly different from those in packed-bed porous media, and they are quite similar to those in
400 open-cell foams with cylindrical struts around a porosity of 0.84. Considering the above
401 discussion, we speculate that the discrepancy between the calculated and measured pressure
402 drops occurs because the differences in both $S_{v,\,solid}$ and ε between the heat-transfer tube
403 samples used in the present study and those used in Ref. [13] results in differences in α and
404 K. The present CFD simulations using X-ray CT can reasonably predict both C and K, even
405 though no detailed information concerning $S_{v,\,solid}$ and ε was identified in an earlier study
406 [13]. Furthermore, we speculate that a deviation of (α, β) between the results of this study
407 and those by Inayat et al. [53,56] may be ascribed to the difference in the averaged tortuous
408 flow-path length, which is closely related to the geometric parameters（$S_{v,\,solid}$ and ε) and the
409 heterogeneous gap distribution within the heat-transfer tube. To improve the prediction
410 accuracy of (α, β), the effects of the intricate fluid-flow trajectory associated with the
411 geometric tortuosity of the porous structure, $S_{v,\,solid}$, and ε on (α, β) must be examined.
412 Figure 8 shows a comparison of the calculated amount of transferred heat Q with the
413 experimental values reported in Ref. [14]. In the present simulation, Q was estimated from

414 the total heat-transfer rate over the entire wall surface area available for heat transfer, and Q
415 increased with the increase in L in the region having a high air mass-flow rate. This result
416 suggests that the heat exchange is not maximized at an air-flow rate of 1.5 g/s for the tube
417 having a size of ∅18 × 50 mm. Further, good quantitative agreements between the
418 calculations and experimental results were observed despite the differences in the samples
419 used in our study and that of Ref. [14].
420
421 **4. Discussion**
422 As discussed in Section 3.1, the solid-phase thermal conduction between the Al
423 fibers and outer wall of the heat-transfer tube contributes to the high heat exchange between
424 the air and Al fibers. To examine the importance of solid-phase thermal conduction on the
425 heat-transfer performance, an Al heat-transfer tube having an idealized wire mesh structure
426 was modeled. Moreover, the interfacial thermal conductivity between the Al fibers and the
427 inner wall of the heat-transfer tube was introduced to the simulation model, and the effect of
428 interfacial thermal conduction on the heat-transfer performance was numerically examined.
429 Figure 9 shows the generated computational model of the Al heat-transfer tube
430 having an idealized wire mesh structure, procedure used for the development of the 25-mm-
431 long heat-transfer tube model, and generated CFD model of the 25-mm-long heat-transfer
432 tube. The Al heat-transfer tube having an idealized wire mesh structure contained Al fibers
433 having widths and thicknesses of 0.3 and 0.3 mm, respectively, and was generated as shown
434 in Figure 9(a). The 0.5-mm-long heat-transfer tube had approximately 80 % porosity, and the
435 25-mm-long heat-transfer tube model was composed of 50 0.5-mm-long heat-transfer tubes.
436 The 25-mm-long heat-transfer tube model has a specific solid surface area of 13500 m^{-1} and a
437 specific fluid surface area of 3500 m^{-1}. Each tube was stacked in the axial (z) direction and
438 rotated at 30° with respect to its neighbor, as shown in Figure 9(b). Approximately 50 million
439 computational cells were used in the CFD simulation for the heat-transfer tube having a size

of ∅18 × 25 mm. The CFD model setup and boundary conditions were the same as those described in Section 2. The constant mass-flow rates in the simulation were 0.5 and 1.0 g/s.

In this CFD model, the interfacial thermal conductivity between the Al fibers and the inner wall of the heat-transfer tube was introduced using the shell conduction model in the Ansys Fluent framework. This interfacial region is called the shell region and is indicated by the red line in Figure 9(a). In this shell region, a constant thermal conductivity of 0.3 W/mK was used, which was comparable to the thermal conductivity of air. The constant thickness of the shell region was introduced as the input parameter and ranged from 1 to 10 μm. The effect of the shell-region thickness on the heat-transfer performance was also examined.

Figure 10 shows typical results of the calculation of the cross-sectional temperature and air-flow velocity contours when the interfacial thermal conductivity between the Al fibers and tube inner wall was assumed to be zero. Similar to Figure 6(a), Figure 10(a) shows the Al fiber portion as a relatively lower-temperature contour owing to the contribution of the solid-phase thermal conduction between the Al fibers and the outer wall of the heat-transfer tube. Comparing Figures 6(a) with 10(a), both the air and Al fibers have a lower temperature in the downstream region of the heat-transfer tube with the idealized wire mesh structure; hence, the idealized wire mesh structure is expected to achieve higher heat exchange than that of the sintered fibrous high-porosity medium.

As shown in Figure 10(b), the air passes through the narrow gap between the wire mesh with a relatively high velocity and then bifurcates after collision with the Al fibers. Compared to that shown in Figure 6(b), the local high-velocity regions are evenly distributed throughout the heat-transfer tube as a result of the designed constant narrow gap of the wire mesh. As discussed in Section 3.1, the air flow at higher velocities is expected to achieve higher heat exchange with the Al fibers owing to convective heat transfer despite the larger pressure drop owing to the friction loss within the narrow gaps.

The pressure drop and Q in the heat-transfer tube having an idealized Al wire mesh structure at 0.5 g/s were estimated to be 0.00844 kPa/mm and 101.3 W, respectively, by CFD simulation. However, these quantities were estimated to be 0.00404 kPa/mm and 97.88 W, respectively, in the case of the sintered fibrous high-porosity medium. Therefore, the heat-transfer tube having an idealized wire mesh structure exhibited superior heat-exchange performance than that filled with the sintered fibrous high-porosity medium. The same superior heat-transfer performance in terms of pressure drop and Q was obtained at 1.0 g/s: 0.0147 kPa/mm and 179.8 W for the sintered fibrous high-porosity media but 0.03101 kPa/mm and 201.3 W for the idealized wire mesh structure. Therefore, the idealized Al wire mesh structure, which could be fabricated through additive manufacturing (for example, metal 3D printing), is expected to overcome the aforementioned disadvantages of sintered fibrous high-porosity media because additive manufacturing can precisely control the gap distribution within the heat-transfer tube. Thus, we believe that the idealized Al wire mesh structure is a promising candidate, especially if prepared through additive manufacturing, for achieving superior heat-exchange performance with better reproducibility. This superior heat-exchange performance of the idealized Al wire mesh structure may be also ascribed to the Ergun parameters (α, β), which are closely related to the intricate fluid-flow trajectory associated with the geometric parameters of a porous structure. The overall heat-transfer performance has been frequently analyzed in terms of an efficiency factor, which is defined by the Colburn number (or Nusselt number) and the frictional factor [30,35]. Because the frictional factor is dependent on the Ergun parameters (α, β), the efficiency factor is also dependent on geometric parameters such as $S_{v,\,solid}$ and ε. To optimize the Ergun parameters (α, β) to achieve superior heat-transfer performance, it is necessary to examine the effects of the Ergun parameters (α, β) and geometric parameters of the porous structure on the efficiency factor, which will be considered in a future study.

Further, the effect of the interfacial thermal conduction between the Al fibers and the inner tube wall surface on the heat-transfer performance was examined. Figure 11 shows the dependence of the calculated cross-sectional temperature contours on the shell-region thickness at 0.5 g/s. As shown, with the increase in the shell-region thickness, the radial heat transfer from the Al fibers toward the tube outer wall is attenuated as a result of the low thermal conductivity of the shell region, which results in a higher temperature in both the downstream air and Al fibers.

Figure 12 shows the dependence of both the pressure drop and Q on the thickness of the shell region at 0.5 g/s. The left and right vertical axes indicate the pressure drop and Q, respectively. As shown, the pressure drop increases slightly with the increase in shell thickness. This is because when the shell is thicker, the air has a higher temperature, and the viscosity of the air increases with temperature, which results in a large friction loss. In contrast to the dependence of the pressure drop on the shell thickness, Q clearly decreased with increasing shell thickness. This is because the low thermal conductivity of the shell region dampens the solid-phase thermal conduction between the Al fibers and tube outer wall, resulting in inferior heat-exchange performance. An earlier study [50] also reported that a narrow constant gap of 0.25 mm heavily impacted the thermal performance when high thermal conductive materials were employed for heat exchanger manufacturing. The present CFD simulations clearly indicate that even a very narrow gap of 5 to 10 μm heavily impacts the heat-exchange performance, and the connectivity between the Al fibers and inner wall of the heat-transfer tube is therefore a key factor affecting heat-exchange performance. In particular, the high heat-exchange performance of the Al heat-transfer tubes filled with sintered fibrous high-porosity media manufactured at the MMC can be attributed to the good connectivity between the Al fibers and the tube inner wall.

5. Conclusion

In the present study, we numerically calculated the fluid flow and temperature fields over the whole structure of a heat-transfer tube filled with a sintered fibrous high-porosity medium using a CFD model based on X-ray CT data. Calculated pressure drop, the amount of heat transferred, the form coefficient C, and the permeability K were compared with earlier studies [13,14], and the discrepancies was discussed according to the Ergun equation. To examine the importance of solid-phase thermal conduction on the heat-transfer performance, an Al heat-transfer tube having an idealized wire mesh structure was modeled, where the interfacial thermal conductivity between the Al fibers and the inner wall of the heat-transfer tube was introduced. Major conclusions of this study are listed as below.

- Calculated pressure drop, the amount of heat transferred, and the form coefficient C corresponded well with the results of previous experimental studies. The estimated permeability K via present CFD simulation were slightly larger than the measured ones. Based on the quantitative investigation according to Ergun equation, we speculated that the difference in K occurs because the differences in both $S_{v,\,solid}$ and ε between the heat-transfer tube samples used in the present study and those used in previous experimental study.
- The differences in both C and K estimated via present CFD simulations between two different samples can be reasonably explained by the slight differences in both $S_{v,\,solid}$ and ε. α value in the Ergun equation was more sensitive to slight differences in $S_{v,\,solid}$ and ε than β, which was a key parameter to estimate the permeability. The higher α value was required to achieve lower pressure drop and lower permeability.
- The results of the CFD simulations revealed that even a very narrow gap of 5 to 10 μm heavily impacted the heat-exchange performance because of the low thermal conductivity of the shell region, and the connectivity between the Al

fibers and inner wall of the tube was a key factor in obtaining high heat-exchange performance.

- The heat-transfer tube having an idealized wire mesh structure exhibited superior heat-exchange performance compared to that filled with a sintered fibrous high-porosity medium. We speculated such superior performance of the idealized Al wire mesh structure may be ascribed to the presence of Ergun parameters that are more suitable for obtaining a high heat-exchange performance than those filled with a sintered fibrous high-porosity medium.

The present CFD simulation can reasonably predict both *C* and *K*. However, further investigations into the relationship between the Ergun parameters, the averaged flow path associated with the geometric parameters of the porous structure, and the heterogeneous gap distribution within the heat-transfer tube are required to improve the prediction accuracy for the pressure drop associated with both *C* and *K*. Furthermore, the effect of the Ergun parameters on the efficiency factor associated with the heat-transfer performance concerning nondimensional analysis was not disclosed systematically in the present research. These investigations are currently in progress.

Acknowledgements

This work was performed at the MMC-NIMS Center of Excellence for Materials Informatics Research. We would like to thank Editage for English language editing.

Conflicts of interest

There are no conflicts of interest to declare.

Author contributions

568 **S. Kawai**: Conceptualization, Data curation, Formal Analysis, Investigation, Methodology,
569 Software, Validation, Visualization, Funding acquisition, Project administration, Resources,
570 Writing–original draft, Writing–review and editing. **I. Watanabe**: Conceptualization,
571 Methodology, Supervision, Project administration, Resources, Writing–review and editing.
572
573 **References**

574 [1] S.Y. Kim, B.H. Kang, J.H. Kim, Forced convection from aluminum foam materials in
575 an asymmetrically heated channel, Int. J. Heat Mass Transf. 44 (2001) 1451–1454.
576 https://doi.org/10.1016/S0017-9310(00)00187-3.

577 [2] J.S. Noh, K.B. Lee, C.G. Lee, Pressure loss and forced convective heat transfer in an
578 annulus filled with aluminum foam, Int. Commun. Heat Mass Transf. 33 (2006) 434–
579 444. https://doi.org/10.1016/j.icheatmasstransfer.2005.11.003.

580 [3] G. Bamorovat Abadi, K.C. Kim, Experimental heat transfer and pressure drop in a
581 metal-foam-filled tube heat exchanger, Exp. Therm. Fluid Sci. 82 (2017) 42–49.
582 https://doi.org/10.1016/j.expthermflusci.2016.10.031.

583 [4] J. Tian, T. Kim, T.J. Lu, H.P. Hodson, D.T. Queheillalt, D.J. Sypeck, H.N.G. Wadley,
584 The effects of topology upon fluid-flow and heat-transfer within cellular copper
585 structures, Int. J. Heat Mass Transf. 47 (2004) 3171–3186.
586 https://doi.org/10.1016/j.ijheatmasstransfer.2004.02.010.

587 [5] W.T. Wu, J.F. Liu, W.J. Li, W.H. Hsieh, Measurement and correlation of hydraulic
588 resistance of flow through woven metal screens, Int. J. Heat Mass Transf. 48 (2005)
589 3008–3017. https://doi.org/10.1016/j.ijheatmasstransfer.2005.01.038.

590 [6] A. Kołodziej, J. Łojewska, M. Jaroszyński, A. Gancarczyk, P. Jodłowski, Heat transfer
591 and flow resistance for stacked wire gauzes: Experiments and modelling, Int. J. Heat
592 Fluid Flow. 33 (2012) 101–108. https://doi.org/10.1016/j.ijheatfluidflow.2011.11.006.

593 [7] M. Iwaniszyn, K. Sindera, A. Gancarczyk, M. Korpyś, R.J. Jędrzejczyk, A. Kołodziej,
594 P.J. Jodłowski, Experimental and CFD investigation of heat transfer and flow
595 resistance in woven wire gauzes, Chem. Eng. Process. - Process Intensif. 163 (2021)
596 108364. https://doi.org/10.1016/j.cep.2021.108364.

597 [8] P.X. Jiang, Z. Wang, Z.P. Ren, B.X. Wang, Experimental research of fluid flow and
598 convection heat transfer in plate channels filled with glass or metallic particles, Exp.
599 Therm. Fluid Sci. 20 (1999) 45–54. https://doi.org/10.1016/S0894-1777(99)00030-8.

600 [9] P.X. Jiang, M.H. Fan, G.S. Si, Z.P. Ren, Thermal-hydraulic performance of small scale
601 micro-channel and porous-media heat-exchangers, Int. J. Heat Mass Transf. 44 (2001)
602 1039–1051. https://doi.org/10.1016/S0017-9310(00)00169-1.

603 [10] T.M. Jeng, S.C. Tzeng, Y.C. Chen, Thermal characteristics in asymmetrically heated
604 channels fully filled with brass beads, Int. J. Therm. Sci. 50 (2011) 1853–1860.
605 https://doi.org/10.1016/j.ijthermalsci.2011.05.011.

606 [11] W. Zhang, X. Bai, M. Bao, A. Nakayama, Heat transfer performance evaluation based
607 on local thermal non-equilibrium for air forced convection in channels filled with
608 metal foam and spherical particles, Appl. Therm. Eng. 145 (2018) 735–742.
609 https://doi.org/10.1016/j.applthermaleng.2018.09.097.

610 [12] L. Tadrist, M. Miscevic, O. Rahli, F. Topin, About the use of fibrous materials in
611 compact heat exchangers, Exp. Therm. Fluid Sci. 28 (2004) 193–199.
612 https://doi.org/10.1016/S0894-1777(03)00039-6.

613 [13] K. Enoki, T. Kobayashi, R. Watanabe, Y. Otomo, A. Akisawa, I. Yaningsih, B.
614 Kristiawan, A.T. Wijayanta, Correlation of pressure drop in the sintered fibrous porous
615 tube with permeability and friction coefficient, IOP Conf. Ser. Mater. Sci. Eng. 1096
616 (2021) 012005. https://doi.org/10.1088/1757-899x/1096/1/012005.

617 [14] R. Watanabe, T. Kobayashi, Y. Otomo, A. Akisawa, Y. Ueda, K. Enoki, Experimental
618 investigation into the heat transfer and pressure drop performance of sintered high
619 porosity media, Appl. Therm. Eng. 196 (2021) 117284.
620 https://doi.org/10.1016/j.applthermaleng.2021.117284.

621 [15] F. Panerai, J.D. White, T.J. Cochell, O.M. Schroeder, N.N. Mansour, M.J. Wright, A.
622 Martin, Experimental measurements of the permeability of fibrous carbon at high-
623 temperature, Int. J. Heat Mass Transf. 101 (2016) 267–273.
624 https://doi.org/10.1016/j.ijheatmasstransfer.2016.05.016.

625 [16] M. Raudenský, I. Astrouski, M. Dohnal, Intensification of heat transfer of polymeric
626 hollow fiber heat exchangers by chaotisation, Appl. Therm. Eng. 113 (2017) 632-638.
627 https://doi.org/10.1016/j.applthermaleng.2016.11.038.

628 [17] B. Dietrich, W. Schabel, M. Kind, H. Martin, Pressure drop measurements of ceramic
629 sponges—Determining the hydraulic diameter, Chem. Eng. Sci. 64 (2009) 3633-3640.
630 https://doi.org/10.1016/j.ces.2009.05.005.

[18] K. Boomsma, D. Poulikakos, Y. Ventikos, Simulations of flow through open cell metal foams using an idealized periodic cell structure, Int. J. Heat Fluid Flow. 24 (2003) 825–834. https://doi.org/10.1016/j.ijheatfluidflow.2003.08.002.

[19] A. Kopanidis, A. Theodorakakos, E. Gavaises, D. Bouris, 3D numerical simulation of flow and conjugate heat transfer through a pore scale model of high porosity open cell metal foam, Int. J. Heat Mass Transf. 53 (2010) 2539–2550. https://doi.org/10.1016/j.ijheatmasstransfer.2009.12.067.

[20] M. Bai, J.N. Chung, Analytical and numerical prediction of heat transfer and pressure drop in open-cell metal foams, Int. J. Therm. Sci. 50 (2011) 869–880. https://doi.org/10.1016/j.ijthermalsci.2011.01.007.

[21] T. Tang, H. Wang, C. Huang, Pore-scale numerical simulation of the heat transfer and fluid flow characteristics in metal foam under high Reynolds numbers based on tetrakaidecahedron model, Int. J. Therm. Sci. 184 (2023) 107903. https://doi.org/10.1016/j.ijthermalsci.2022.107903

[22] Z. Nie, Y. Lin, Q. Tong, Numerical investigation of pressure drop and heat transfer through open cell foams with 3D Laguerre-Voronoi model, Int. J. Heat Mass Transf. 113 (2017) 819–839. https://doi.org/10.1016/j.ijheatmasstransfer.2017.05.119.

[23] K. Yang, K. Liu, J. Wang, Pore-scale numerical simulation of convection heat transfer in high porosity open-cell metal foam under rotating conditions, Appl. Therm. Eng. 195 (2021) 117168. https://doi.org/10.1016/j.applthermaleng.2021.117168.

[24] R. N. Konduru, O. Farges, V. Schick, P. Hairy, Y. Gaillard, G. Parent, Experimental and numerical investigation of porous heat exchangers with Kelvin cell structured

foam at high temperatures: Coupled conduction-convection and radiation heat transfer, Int. J. Heat Mass Transf. 224 (2024) 125253. https://doi.org/10.1016/j.ijheatmasstransfer.2024.125253

[25] J. Iyer, T. Moore, D. Nguyen, P. Roy, J. Stolaroff, Heat transfer and pressure drop characteristics of heat exchangers based on triply periodic minimal and periodic nodal surfaces, Appl. Therm. Eng. 209 (2022) 118192. https://doi.org/10.1016/j.applthermaleng.2022.118192.

[26] T. Dixit, E. Al-Hajri, M. C. Paul, P. Nithiarasu, S. Kumar, High performance, microarchitected, compact heat exchanger enabled by 3D printing, Appl. Therm. Eng. 210 (2022) 118339. https://doi.org/10.1016/j.applthermaleng.2022.118339.

[27] K. Yan, J. Wang, L. Li, H. Deng, Numerical investigation into thermo-hydraulic characteristics and mixing performance of triply periodic minimal surface-structured heat exchangers, Appl. Therm. Eng. 230 (2023) 120748. https://doi.org/10.1016/j.applthermaleng.2023.120748.

[28] W. Tang, C. Zou, H. Zhou, L. Zhang, Y. Zeng, L. Sun, Y. Zhao, M. Yan, J. Fu, J. Hu, Z. Li, Z. Liu, T. Wang, Z. Zhang, A novel convective heat transfer enhancement method based on precise control of Gyroid-type TPMS lattice structure, Appl. Therm. Eng. 230 (2023) 120797. https://doi.org/10.1016/j.applthermaleng.2023.120797.

[29] S. Samson, P. Tran, P. Marzocca, Design and modelling of porous gyroid heatsinks: Influences of cell size, porosity and material variation, Appl. Therm. Eng. 235 (2023) 121296. https://doi.org/10.1016/j.applthermaleng.2023.121296.

[30] C. Moon, H.D. Kim, K.C. Kim, Kelvin-cell-based metal foam heat exchanger with elliptical struts for low energy consumption, Appl. Therm. Eng. 144 (2018) 540–550. https://doi.org/10.1016/j.applthermaleng.2018.07.110.

[31] M. Calati, E. De Monte, S. Mancin, Numerical analysis of the effects of the structure shape and orientation of kelvin cell porous structures during air forced convection, Appl. Sci. 11 (2021) 6189. https://doi.org/10.3390/app11136189.

[32] G. Ambrosio, N. Bianco, W.K.S. Chiu, M. Iasiello, V. Naso, M. Oliviero, The effect of open-cell metal foams strut shape on convection heat transfer and pressure drop, Appl. Therm. Eng. 103 (2016) 333–343. https://doi.org/10.1016/j.applthermaleng.2016.04.085.

[33] A. Della Torre, G. Montenegro, G.R. Tabor, M.L. Wears, CFD characterization of flow regimes inside open cell foam substrates, Int. J. Heat Fluid Flow. 50 (2014) 72–82. https://doi.org/10.1016/j.ijheatfluidflow.2014.05.005.

[34] S.M. Richardson, Fluid mechanics., Mech. Eng. Ser. (1989) 15–113. https://doi.org/10.1007/978-1-4684-0412-8_2.

[35] Bejan A, Kraus AD. Porous media. In: Heat Transfer Handbook. Hoboken, New Jersey: John Wiley & Sons, Inc.; 2003. p. 1029–1180.

[36] P. Ranut, E. Nobile, L. Mancini, High resolution microtomography-based CFD simulation of flow and heat transfer in aluminum metal foams, Appl. Therm. Eng. 69 (2014) 230–240. https://doi.org/10.1016/j.applthermaleng.2013.11.056.

[37] S. Meinicke, C.O. Möller, B. Dietrich, M. Schlüter, T. Wetzel, Experimental and numerical investigation of single-phase hydrodynamics in glass sponges by means of

combined μPIV measurements and CFD simulation, Chem. Eng. Sci. 160 (2017) 131–143. https://doi.org/10.1016/j.ces.2016.11.027.

[38] T. Dixit, I. Ghosh, Simulation intricacies of open-cell metal foam fin subjected to convective flow, Appl. Therm. Eng. 137 (2018) 532–544. https://doi.org/10.1016/j.applthermaleng.2018.04.011.

[39] R. Wang, A.P. Hou, Z. Wu, Tomography-based investigation of flow and heat transfer inside reticulated porous ceramics, Appl. Therm. Eng. 184 (2021) 116115. https://doi.org/10.1016/j.applthermaleng.2020.116115.

[40] J. Liu, P. Yu, Y. Li, C. Wan, D. Du, Numerical simulation on convective heat transfer characteristics in porous media based on the digital rock technology, Int. J. Heat Mass Transf. 196 (2022) 123323. https://doi.org/10.1016/j.ijheatmasstransfer.2022.123323.

[41] Z. Zhang, G. Yan, M. Sun, H. Yan, J. Zhao, Y. Song, Y. Liu, Pore-scale simulation of forced convection heat transfer in metal foams with uniform and gradient structures, Appl. Therm. Eng. 225 (2023) 120074. https://doi.org/10.1016/j.applthermaleng.2023.120074.

[42] K. Kuhlmann, C. Sinn, J. M. U. Siebert, G. Wehinger, J. Thöming, G. R. Pesch, From μCT data to CFD: an open-source workflow for engineering applications, Engineering Applications of Computational Fluid Mechanics, 16:1 (2022), 1706-1723. https://doi.org/10.1080/19942060.2022.2109758.

[43] E. Hamidi, P. Ganesan, S.V. Muniandy, M.H. Amir Hassan, Lattice Boltzmann Method simulation of flow and forced convective heat transfer on 3D micro X-ray tomography

of metal foam heat sink, Int. J. Therm. Sci. 172 (2022) 107240. https://doi.org/10.1016/j.ijthermalsci.2021.107240.

[44] Q. Lyu, A. Chen, J. Jia, A. Singh, P. Dai, Fluids flow in granular aggregate packings reconstructed by high-energy X-ray computed tomography and lattice Boltzmann method, Computers & Fluids 253 (2023) 105787. https://doi.org/10.1016/j.compfluid.2023.105787.

[45] Y. Li, Y. Chi, C. Zhao, Y. Miao, S. Han, L. Chen, Modelling fluid flow in carbon fibre porous media based on X-ray microtomography and lattice Boltzmann method, Composite Structures, 300 (2022) 116085. https://doi.org/10.1016/j.compstruct.2022.116085.

[46] M. Sadeghi, M. Mirdrikvand, G.R. Pesch, W. Dreher, J. Thöming, Full-field analysis of gas flow within open-cell foams: comparison of micro-computed tomography-based CFD simulations with experimental magnetic resonance flow mapping data, Exp. Fluids. 61 (2020). https://doi.org/10.1007/s00348-020-02960-4.

[47] M. Mirdrikvand, M. Sadeghi, G.R. Pesch, W. Dreher, J. Thöming, Full-field comparison of MRV and CFD of gas flow through regular catalytic monolithic structures, Processes. 9 (2021) 566. https://doi.org/10.3390/pr9030566.

[48] B. Eisfeld, K. Schnitzlein, The influence of confining walls on the pressure drop in packed beds, Chem. Eng. Sci. 56 (2001) 4321–4329. https://doi.org/10.1016/S0009-2509(00)00533-9.

737 [49] N. Dukhan, M. Ali, Strong wall and transverse size effects on pressure drop of flow
738 through open-cell metal foam, Int. J. Therm. Sci. 57 (2012) 85–91.
739 https://doi.org/10.1016/j.ijthermalsci.2012.02.017.

740 [50] S.A. Zavattoni, L. Cornolti, R. Puragliesi, E. Arrivabeni, A. Ortona, M.C. Barbeto,
741 Conceptual design of an innovative gas–gas ceramic compact heat exchanger suitable
742 for high temperature applications, Heat and Mass Transfer (2022).
743 https://doi.org/10.1007/s00231-022-03284-1

744 [51] Thermo Fisher Scientific. Thermo Scientific Amira-Avizo Software. Website:
745 https://www.thermofisher.com/jp/ja/home/industrial/electron-microscopy/electron-
746 microscopy-instruments-workflow-solutions/3d-visualization-analysis-software.html
747 (accessed on 27 October 2023)

748 [52] Cengel YA, Cimbala JM. Appendix 1 Property Tables and Charts: Table A-9
749 Properties of Air at 1 atm Pressure. In: Fluid Mechanics: Fundamentals and
750 Applications. 4th ed. New York: McGraw-Hill; 2018.

751 [53] A. Inayat, M. Klumpp, M. Lämmermann, H. Freund, W. Schwieger, Development of a
752 new pressure drop correlation for open-cell foams based completely on theoretical
753 grounds: Taking into account strut shape and geometric tortuosity, Chem. Eng. J. 287
754 (2016) 704-719. https://doi.org/10.1016/j.cej.2015.11.050.

755 [54] J. Zhao, M. Sun, L. Zhang, C. Hu, D. Tang, L. Yang, Y. Song, Forced convection heat
756 transfer in porous structure: effect of morphology on pressure drop and heat transfer
757 coefficient, J. Therm. Sci. 30, 363–393 (2021). https://doi.org/10.1007/s11630-021-
758 1403-x.

759 [55] S. Ergun, Fluid Flow through Packed Columns, Chem. Eng. Prog. 48 (2), 89–94
760 (1952).

761 [56] A. Inayat, H. Freund, A. Schwab, T. Zeoser, W. Schwieger, Predicting the Specific
762 Surface Area and Pressure Drop of Reticulated Ceramic Foams Used as Catalyst
763 Support, Adv. Eng. Mater. 13 (2011) 990-995.
764 https://doi.org/10.1002/adem.201100038.

765

766

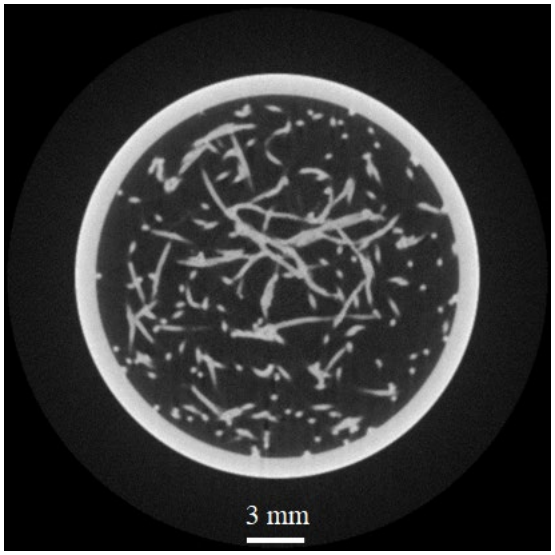

Figure 1. Cross-sectional image of the Al heat-transfer tube filled with the sintered fibrous high-porosity medium obtained using X-ray CT.

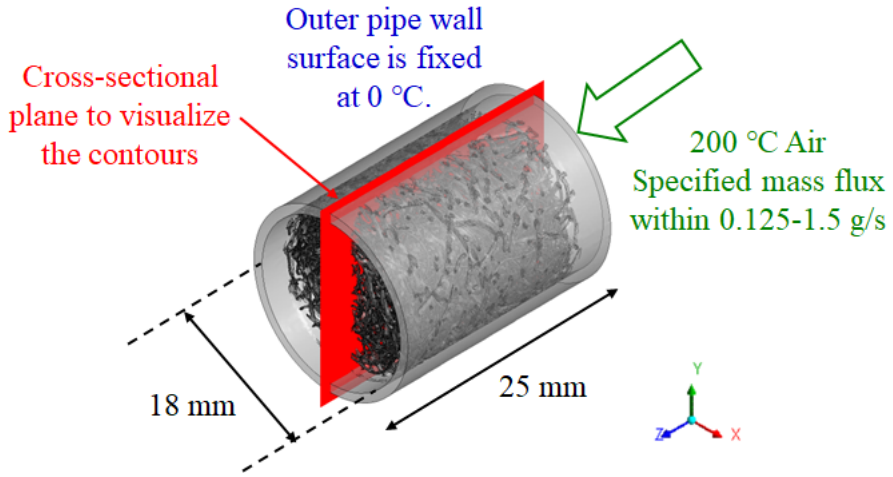

771

772 Figure 2. CFD model of the Al heat-transfer tube filled with the sintered fibrous high-

773 porosity medium generated from the X-ray CT data. The boundary conditions for the model

774 are also specified.

775

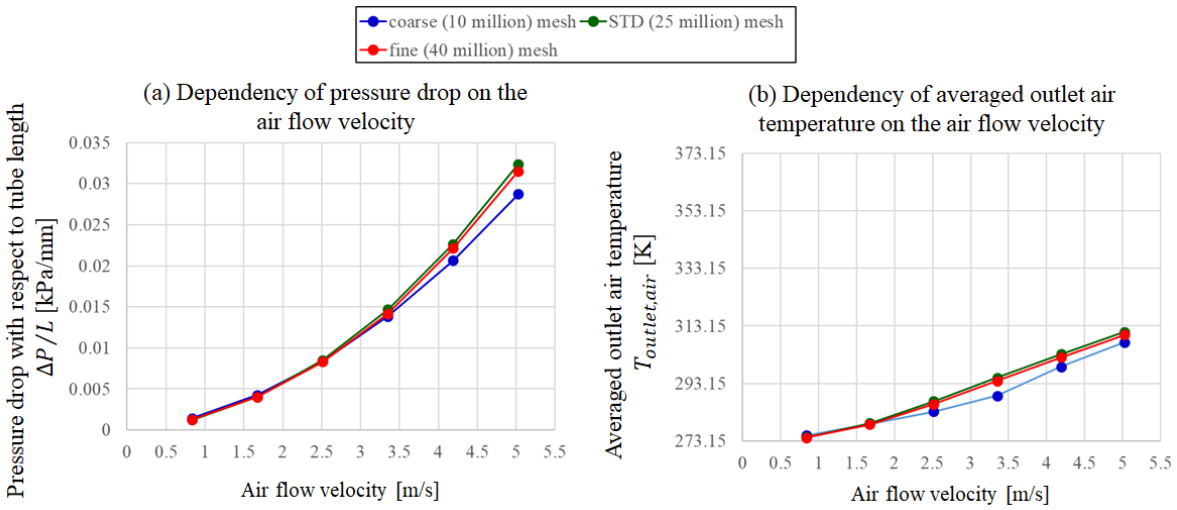

776

777 Figure 3. Comparison of (a) pressure drop with respect to tube length and (b) averaged outlet

778 air temperature among three CFD models with different computational grid sizes for the heat-

779 transfer tube having a size of ∅18 × 25 mm.

780

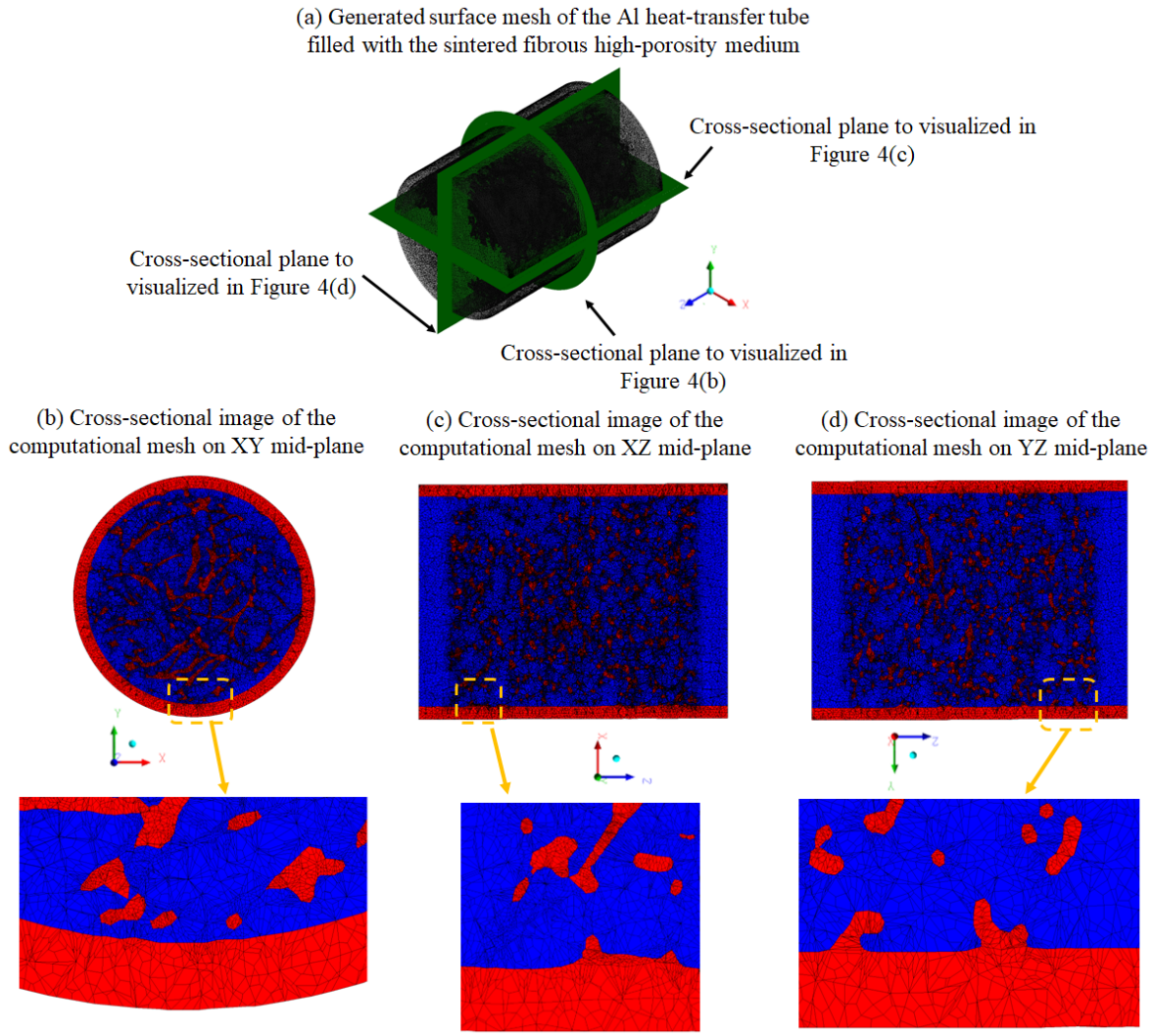

781

782 Figure 4. Details of the computational cell used for the Al heat-transfer tube filled with the
783 sintered fibrous high-porosity medium having a size of ∅18 × 25 mm. (a) Generated surface
784 mesh of Al heat-transfer tube, (b)-(d): typical visualizations of cross-sectional computational
785 mesh in XY, XZ, and XZ mid-planes.

786

787

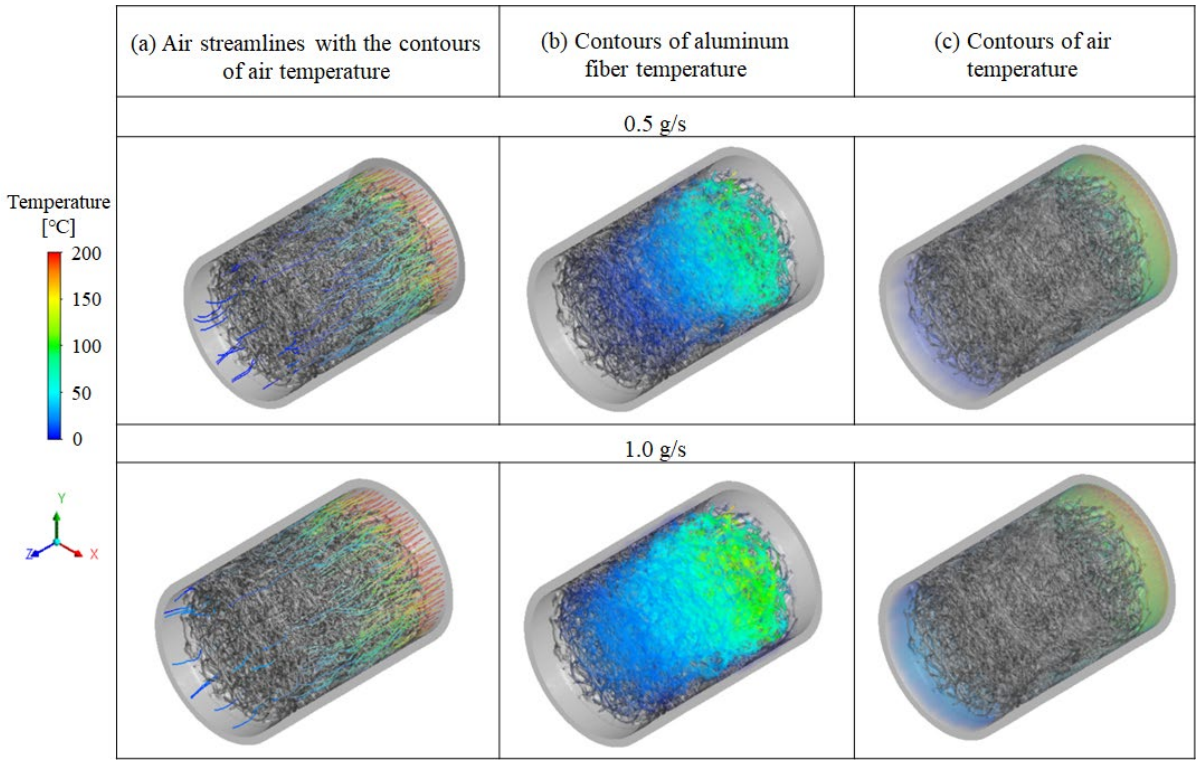

Figure 5. Computed air-flow patterns and temperature contours in the Al heat-transfer tube having a size of ∅18 × 25 mm at different air flow rates of 0.5 and 1.0 g/s. (a) Streamlines of the air flow through the heat-transfer tube, (b) temperature contours of Al fibers, and (c) temperature contours of air within the heat-transfer tube.

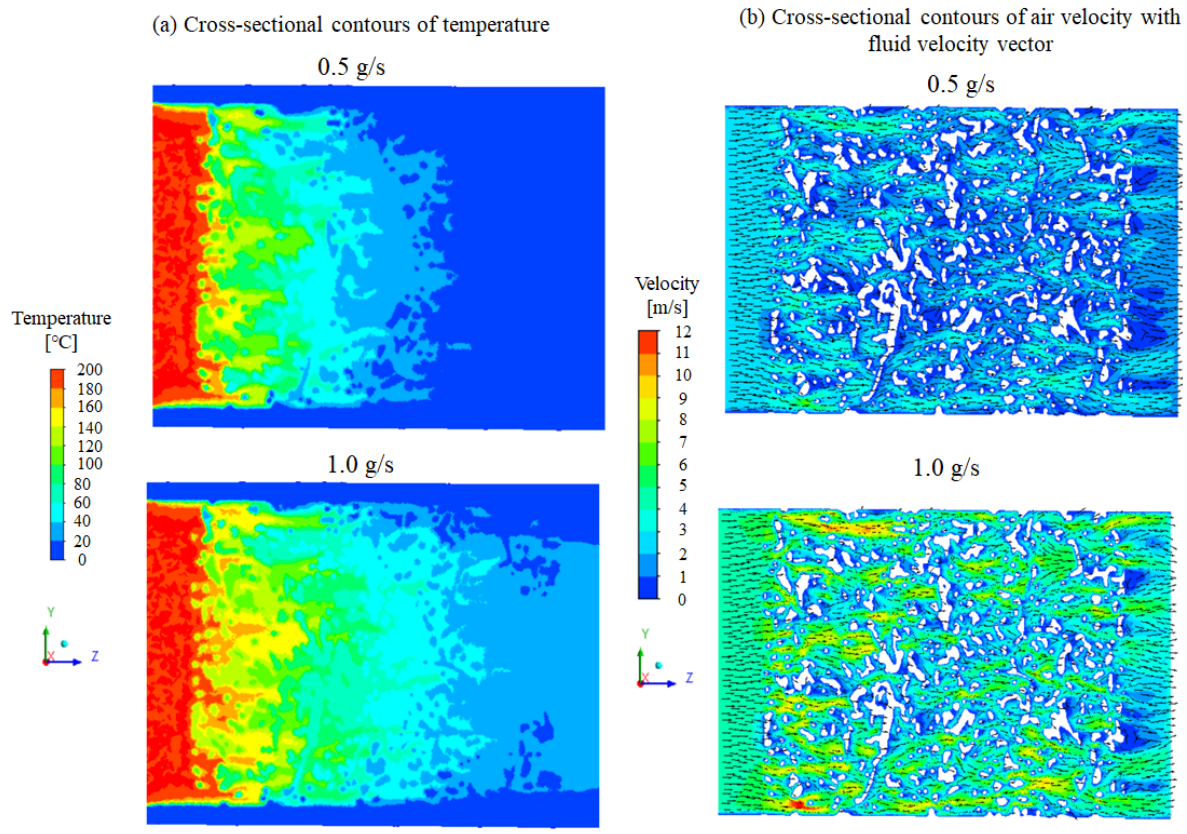

Figure 6. Calculated cross-sectional temperature and air-flow velocity contours for the Al heat-transfer tube of size ∅18 × 25 mm at air-flow rates of 0.5 and 1.0 g/s. (a) Cross-sectional temperature contour and (b) cross-sectional contour of the fluid velocity. The fluid velocity vector is represented by the black arrow.

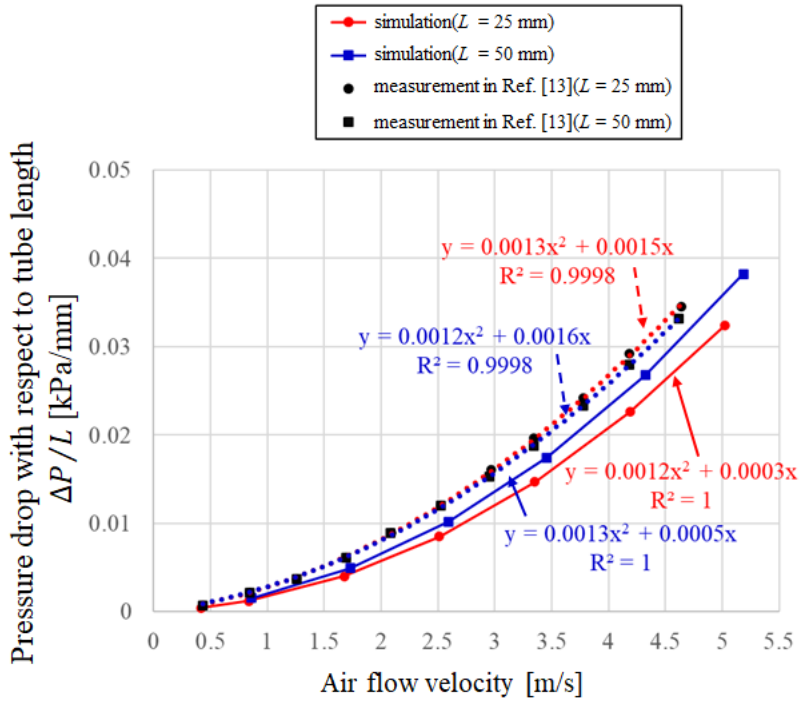

802

803 Figure 7. Comparison of the pressure drops obtained numerically (present work) and

804 experimentally [13]. The abscissa represents the air-flow velocity estimated by the mass-flow

805 rate between 0.125 and 1.5 g/s. The sizes of the heat-transfer tubes were ∅18 × 25 mm and

806 ∅18 × 50 mm. The dotted lines are approximations to the experimental measurements.

807

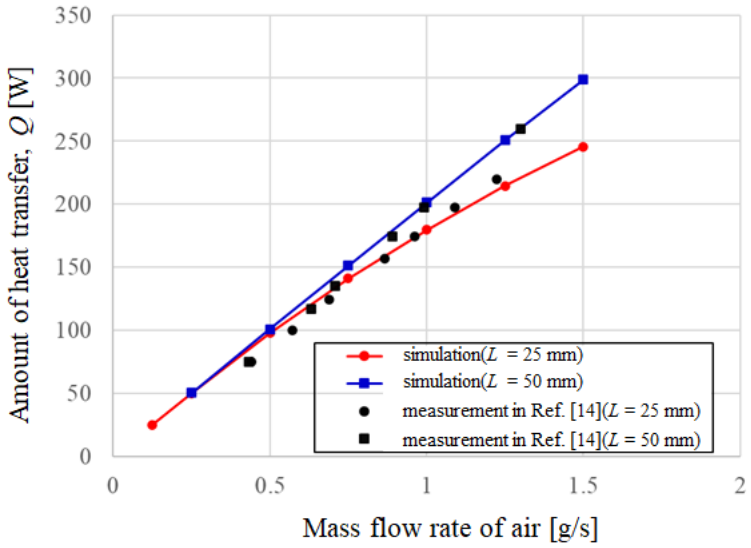

808

809 Figure 8. Comparison of amount of heat transferred (Q) at different air-flow rates obtained

810 numerically (present work) and experimentally [14].

811

812

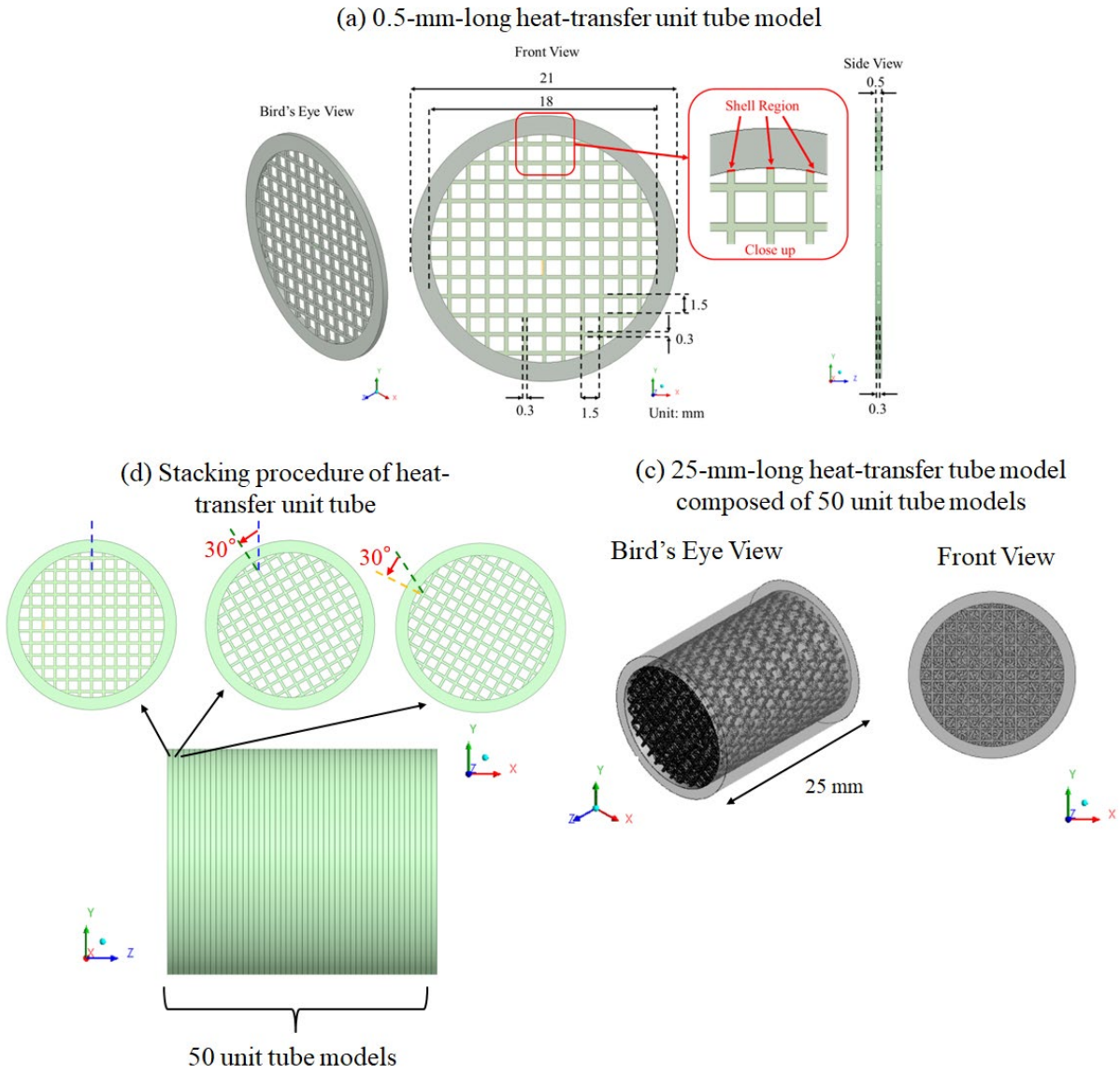

Figure 9. Generated computational model of the Al heat-transfer unit tube containing an idealized wire mesh structure and 25-mm-long heat-transfer tube model in which the unit tubes are stacked and rotated 30° with respect to the next. (a) 0.5-mm-long heat-transfer unit tube model, (b) stacking procedure for the model containing 50 heat-transfer tubes, and (c) 25-mm-long heat-transfer tube model. In Figure 7(a), the shell region is indicated by a red line. In Figure 7(b), 50 tubes are stacked and rotated 30° with respect to the axial (z) direction.

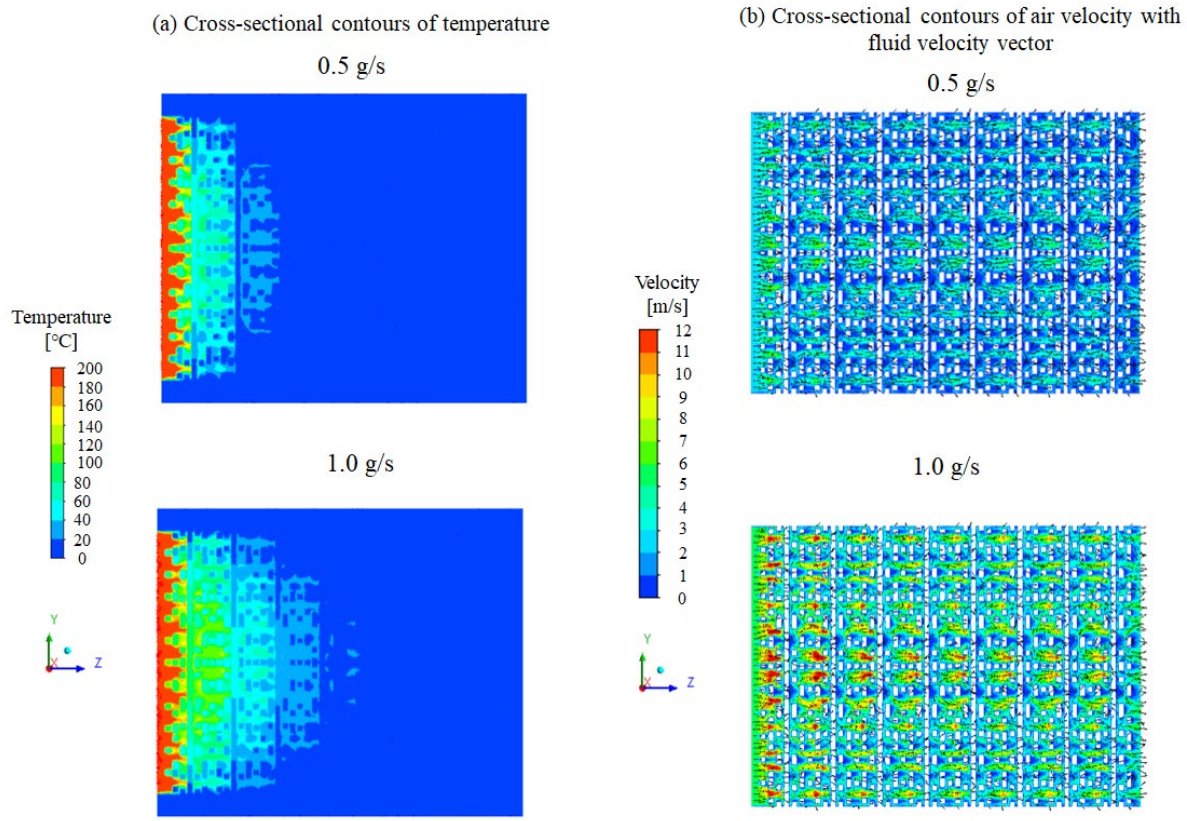

Figure 10. Calculated cross-sectional temperature and air-flow velocity contours at air-flow rates of 0.5 and 1.0 g/s. The interfacial thermal conductivity between the Al fiber and tube inner wall is assumed to be zero. (a) Cross-sectional temperature contours and (b) cross-sectional contours of the fluid velocity. The fluid velocity vector is represented by a black arrow.

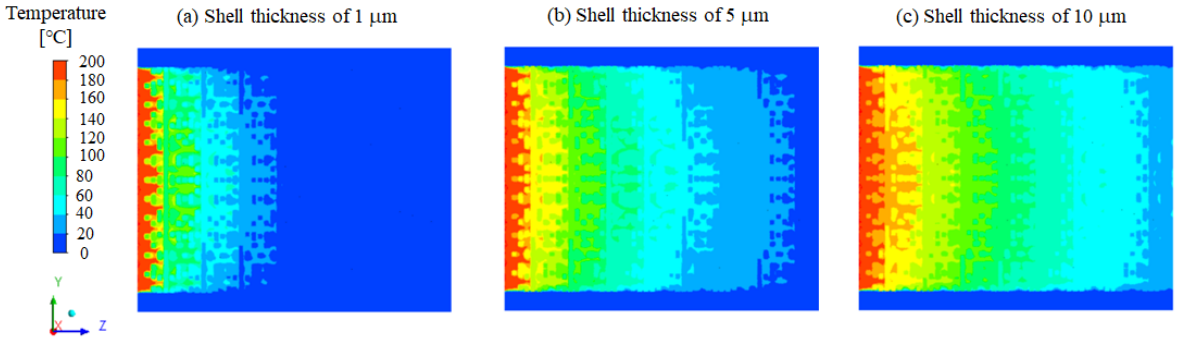

831

832 Figure 11. Dependence of the calculated cross-sectional temperature contours on the shell-

833 region thickness at an air-flow rate of 0.5 g/s.

834

835

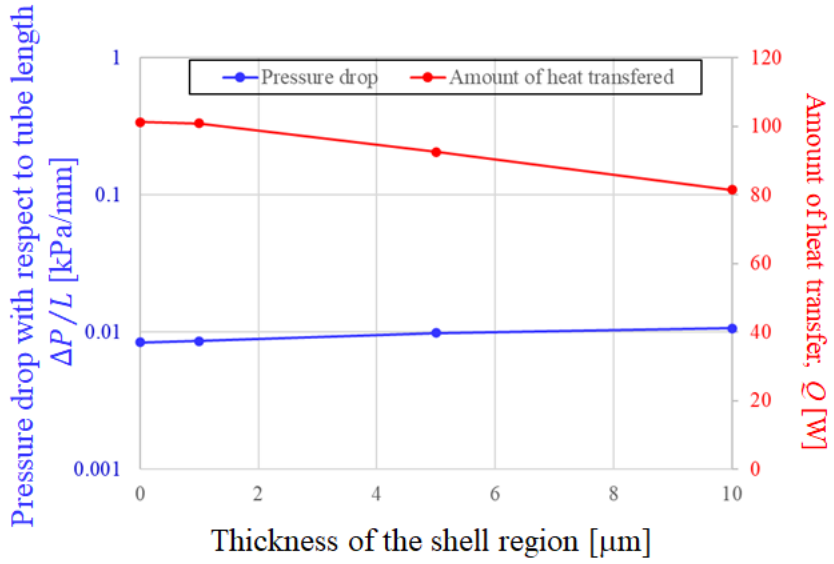

836

837 Figure 12. Changes in the pressure drop and the amount of heat transferred with respect to the

838 thickness of the shell region at an air flow-rate of 0.5 g/s.

839

840

841 Table 1. Geometrical properties of the Al heat transfer tube with a sintered fibrous high-

842 porosity medium used in the present CFD simulations.

	∅18 × 25 mm	∅18 × 50 mm
Specific fluid surface area $S_{v,fluid}$ [m^{-1}]	2274	2527
Specific solid surface area $S_{v,solid}$ [m^{-1}]	11830	12040
Porosity ε [vol%]	0.839	0.827

843

844

845 Table 2. Physical properties of the solid Al phase used in the present CFD simulations.

Density [kg/m^3]	2719
Specific heat capacity [J/(kgK)]	871
Thermal conductivity [W/(mK)]	237

846

847

848 Table 3. Comparison of the form coefficient and permeability between the present CFD

849 simulations and experimental measurements presented in Ref. [13].

	Present simulations		Experiments in Ref. [13]	
	∅18 × 25 mm	∅18 × 50 mm	∅18 × 25 mm	∅18 × 50 mm
Form coefficient C [m^{-1}]	1128	1227	1051	1018
Permeability K [m^2]	5.67×10^{-8}	3.78×10^{-8}	1.25×10^{-8}	1.28×10^{-8}

850

851